An object-based SAR image iceberg detection algorithm applied to the Amundsen Sea

A.K. Mazur [a,b,*], A.K. Wåhlin [a], A. Krężel [b]

[a] Department of Marine Sciences, University of Gothenburg, PO Box 460, 405 30 Göteborg, Sweden
[b] Institute of Oceanography, University of Gdańsk, Al. Marszałka Piłsudskiego 46, 81-836 Gdynia, Poland

ARTICLE INFO

ABSTRACT

An object-based method for automatic iceberg detection from Advanced Synthetic Aperture Radar (ASAR) images has been developed and applied in the Amundsen Sea, Antarctica. The automatic identification is based on brightness and spatial parameters of the ASAR images at five scale levels, and was verified with manual classification in four areas chosen to represent varying environmental conditions. The presented algorithm works comparatively well with images of the ocean in freezing temperatures and strong wind conditions, common in the Amundsen Sea. The detection rate was 96.2% which corresponds to 93.2% of the icebergs area, for all seasons. The algorithm generated 3.8% errors in the form of 'misses' and 7.0% of 'false alarms', mainly caused by the presence of ice floes.

The method was applied on 432 radar images acquired in 2011 under different meteorological, oceanographic and sea ice conditions. As an output a map showing the probability of finding icebergs has been created. It shows that high probability coincides with depth contours and indicates a westward drift of the bergs throughout the whole region.

Contents

1. Introduction

The West Antarctic Ice Sheet is one of Earth's largest reservoirs of ice and it has the potential to influence global sea level (Bamber et al.,

2009). The glaciers that drain the West Antarctic Ice Sheet into the Amundsen Sea are speeding up contributing to the ice mass loss (Paolo et al., 2015; Pritchard et al., 2012; Rignot et al., 2013). Although iceberg calving is a substantial part of the ice volume budget in this area (Depoorter et al., 2013; Liu et al., 2015), focus has historically been on the basal melt induced by ocean currents circulating below the ice shelves (Jacobs et al., 2013, 2011; Pritchard et al., 2012). Large quantities of glacial melt water have been observed in the water column

* Corresponding author at: Department of Marine Sciences, University of Gothenburg, PO Box 460, 405 30 Göteborg, Sweden.
E-mail address: akmazur@marine.gu.se (A.K. Mazur).

on the Amundsen Sea shelf (e.g. Jacobs et al., 2012; Wåhlin et al., 2010), but it is not known whether this melt comes from the ice shelves or from the icebergs already detached from the glaciers. It is not yet known how large the net iceberg melt is in the Amundsen Sea, nor the impact the melt has on the ocean circulation on the shelf. The fate of the icebergs after calving, i.e. how they drift and where and why they accumulate, is also a very recent topic.

Icebergs form through calving at ice shelves and glacier tongues in coastal areas where glaciers terminate in the sea. They have an impact on the local water circulation and primary production (e.g. Biddle et al., 2015; Lancelot et al., 2009; Raiswell et al., 2008; Smith et al., 2007), and also affect sea ice formation. Through iceberg drift large quantities of freshwater are moved into the open sea where thin fresh melt water-enriched surface layers can form as the bergs melt. The amount of freshwater stored in the near-surface water column is a key component of sea ice formation (Bintanja et al., 2015; Björk et al., 2002), which is particularly clear in the Southern Ocean where melting icebergs are often surrounded by a tongue of sea ice. According to Liu et al. (2015) ice mass loss due to iceberg calving in the Amundsen Sea reaches 244 Gt/yr, which is presently the highest rate in Antarctica. The estimated ice mass loss induced by basal melt in the basin is 484 ± 57 Gt/yr and the total grounding line flux 505 ± 24 GT/yr (Depoorter et al., 2013).

Ship observations of icebergs (e.g. Jacka and Giles, 2007; Romanov et al., 2012) can provide detailed information about their size and shape but are temporally and spatially limited. Satellite borne sensors, e.g., radar altimeters, scatterometers or Synthetic Aperture Radars (SAR), can provide data with wide area coverage and a relatively high temporal resolution and are increasingly used in iceberg detection. Various sensors have different limitations. Because of low spatial resolution only very large icebergs (>10 nautical miles along at least one axis) can be monitored with the use of scatterometers (Stuart and Long, 2011). Radar altimeters are limited when deformed sea ice is present (Tournadre et al., 2012, 2008) and optical sensors are restricted by clouds or darkness and can have difficulty distinguishing between snow covered ice floes and icebergs (Fig. 1). SAR sensors can acquire data under almost all meteorological conditions with relatively high spatial resolution and is now commonly used for iceberg detection (e.g. Silva and Bigg, 2005; Wesche and Dierking, 2012; Williams et al., 1999; Willis et al., 1996; Young et al., 1998).

Icebergs are often regions of higher radar backscatter intensity than their surroundings. As the relative dielectric constant value of non-saline ice is low, the attenuation depth of the radar signal at C-band may range from 1 to 14 m, depending on additional scattering caused by air bubbles and other impurities within the berg (Langley et al.,

2007; Rignot et al., 2001). Hence the backscatter of an iceberg is affected by both surface and volume scattering. According to Young et al. (1998) icebergs have backscatter intensity between −6 dB to −4 dB, or higher, while the surroundings (mix of open water and sea ice) have less than −10.5 dB. Silva and Bigg (2005) empirically determined the iceberg threshold value of −10 dB as a lower limit for the average backscatter coefficient. Both studies were based on winter images. The intensity threshold proposed by Willis et al. (1996) is based on resolution-reduced images, combined with mathematical morphology operators. Another type of pixel-based iceberg identification was developed by Wesche and Dierking (2012) in which K-distribution functions were used to identify relative cumulation distributions of icebergs and background from which intensity thresholds were determined. The performance of such algorithms are good when there is high contrast between the iceberg and its surroundings, but less good when the contrast is small e.g. in a rough sea state (Wesche and Dierking, 2012; Williams et al., 1999).

The ability to distinguish icebergs from open water or low concentration sea ice depends on meteorological conditions. If the air temperature is above freezing, the backscatter of icebergs can be significantly decreased due to wet snow or liquid water on the surface of the berg, and they can appear as dark objects against a brighter background (Wesche and Dierking, 2012; Willis et al., 1996). Willis et al. (1996) determined the optimal wind conditions for iceberg detection in open water as the wind speed below 5 m·s^{-1} or above 11 m·s^{-1}. Optimal meteorological conditions for SAR iceberg detection are hence freezing temperature and presence of young saline sea ice without any deformations (Wesche and Dierking, 2012). In such conditions icebergs appear as bright objects against a darker background and can be identified from the backscatter value. In non-optimal meteorological conditions e.g. in wind-roughened open water conditions or the air temperature at or above the melting point it is however more difficult to use pixel-based methods to identify icebergs from SAR images (Wesche and Dierking, 2012; Willis et al., 1996). The Amundsen Sea is characterized by challenging conditions for iceberg detection through existing methods, i.e. strong winds, cold winters and large sea ice drift, acting to form a rough and highly variable sea- or ice surface that has scatter properties comparable to the icebergs themselves. Despite the fact that it is one of the most iceberg-rich seas in Antarctica only a few studies have been done on icebergs in the Amundsen Sea (Wesche and Dierking, 2015).

In recent years there has been growing interest in methods studying groups of pixels rather than single pixels. Segments of pixels are then translated into objects, using state-of-art methods. Williams et al. (1999) and Young et al. (1998) identified icebergs by detecting its
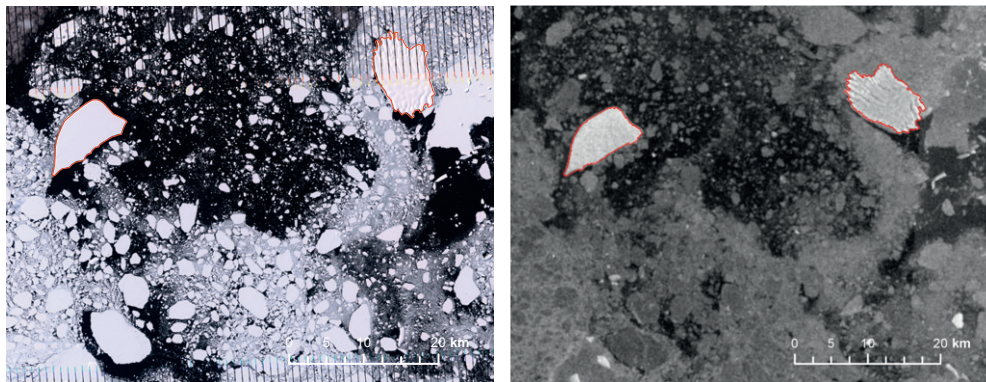

Fig. 1. Comparison of optical LANDSAT ETM+ image, recorded on 29 Dec 2011 (left) and ENVISAT ASAR image, recorded on 30 Dec 2011 (right). Icebergs (red outline) cannot be distinguished from snow covered sea ice floes on the optical image (left) and they can be easily recognized on the corresponding ASAR image (right). Red outlines are digitized icebergs (left) and results of the classification (right).

edges from the backscatter gradient by an algorithm proposed by Sephton et al. (1994). The method is limited to icebergs bigger than 6 pixels and generally overestimates the iceberg area. Silva and Bigg (2005) also utilized an algorithm with edge detection using the multiresolution filter of Fjørtoft et al. (1999). Segments were created using the watershed algorithm (Beucher and Lantuejoul, 1978) and homogenous objects were merged, based on proportion of shared border and average intensity difference between two touching segments. A strength of this method is that the formed objects have spatial information associated with them, e.g., area, perimeter, width, length etc., which can be used during the classification process. To identify icebergs Silva and Bigg (2005) used both backscatter coefficient and geometrical properties. The study showed that spatial features can significantly improve the classification performance, and their algorithm gave better results than the *sigma-on-mu* filter and pixel bonding presented in previous studies (Williams et al., 1999; Young et al., 1998).

More advanced methods for object identification, referred to as Object Based Image Analyses (OBIA), have been developed and applied to e.g. land-use classification (Cleve et al., 2008; Gholoobi et al., 2010; Whiteside et al., 2011) where they have provided substantial improvement. This class of techniques builds on segmentation, edge-detection, feature extraction and classification concepts that are combined to improve the performance. Moreover OBIA is inextricably linked to multi-scale analysis concepts. Multi-scale analysis, i.e. segmentation of objects at multiple scale levels and building a hierarchical network of super- and sub-segments (Baatz and Schäpe, 2000), is an important tool. Each scale layer corresponds to a specific spatial scale of features in the environment, for example, different sizes of icebergs. The multiresolution segmentation algorithm was implemented in the eCognition Developer software around which much of the OBIA development originated (for a review see e.g. Blaschke, 2010). Today, OBIA or GEOBIA (Geographic Object-Based Image Analysis) is a rapidly growing and evolving methodology in remote sensing and GIScience (Blaschke et al., 2014).

We will here for the first time apply OBIA to SAR data in order to classify icebergs. In order to examine whether classifying objects rather than pixels improves classification results in images influenced by speckle noise radar data, the present investigation was undertaken. The study is focused on iceberg detection in the Amundsen Sea, a region in which it is notoriously difficult to detect icebergs due to the prevailing high winds causing sea ice deformations. Parameters based on brightness value and spatial parameters of icebergs in the Amundsen Sea are analyzed, and a methodology for iceberg detection and classification based on the results is presented. We use the new method to calculate the probability of icebergs occurrence in the Amundsen Sea in 2011.

2. Data and study area

For the development of the method 432 ENVISAT ASAR Wide Swath Mode (WSM) Level 1b images recorded between 1 January and 31 December 2011 covering the Amundsen Sea shelf area (Fig. 2) were analyzed. ASAR WSM are medium resolution radar images acquired at C-band (5.3 GHz) and HH or VV polarization using the ScanSAR technique (Envisat ASAR Product Handbook, 2007). They are provided at a pixel size of 75 m × 75 m, with an effective spatial resolution of 150 m × 150 m and incidence angle 17°–43°. For this study only HH polarized data were available.

Air temperature and wind data were taken from the European Centre for Medium-Range Weather Forecasts (ECMWF) ERA interim reanalysis data (Dee et al., 2011; Fig. 2) which according to Bracegirdle and Marshall (2012) is the most accurate of the six major meteorological reanalysis products covering the Amundsen Sea (see also Carvajal et al. (2013) and Wåhlin et al. (2013) for more comparisons of ECMWF wind data in the in the Amundsen Sea region). The Amundsen Sea is characterized by a seasonal ice cover, cold winters and strong winds. Fig. 3 shows the temperature and wind speed in the four control points (Fig. 2). Freezing conditions and strong winds, challenging conditions for iceberg detection, occur in the Amundsen Sea throughout the year. Temperatures above zero degrees Celsius, at which icebergs can appear as dark objects against a bright background in the radar images, were noted in January and December at all four control points. However, the low summertime winds appear to counteract this and dark icebergs against a brighter background were present on only one image, recorded on 24 Dec 2011 and hence not further considered here.

3. Preprocessing of the data

3.1. Reprojection and radiometric calibration

The ASAR WSM Level 1b product includes slant range to ground range correction but the data are not geolocated or radiometrically
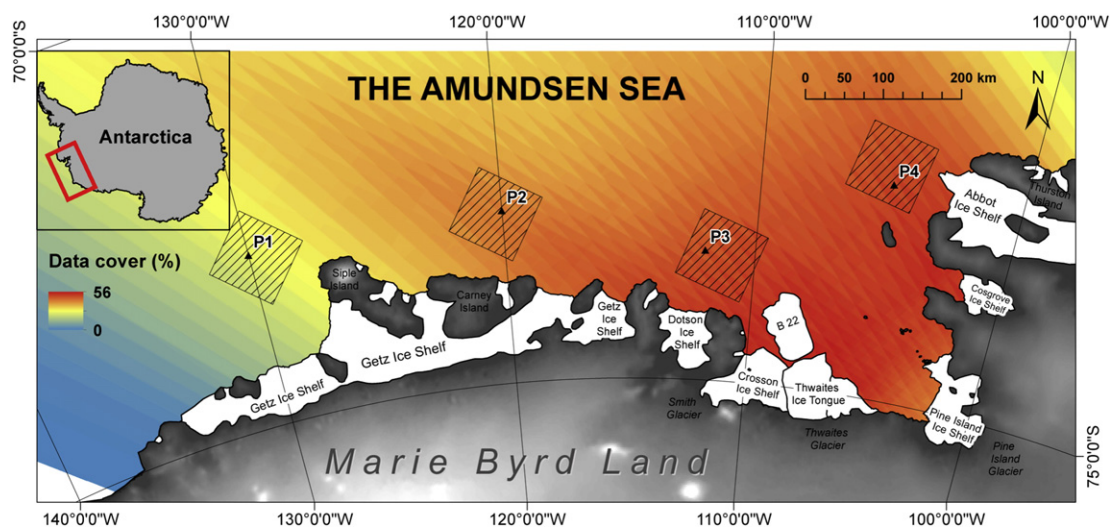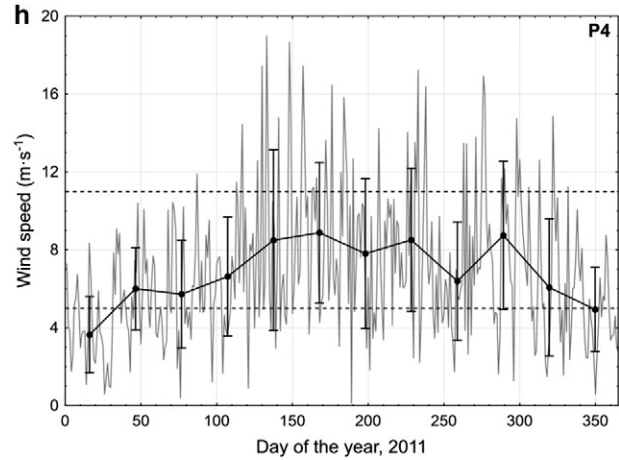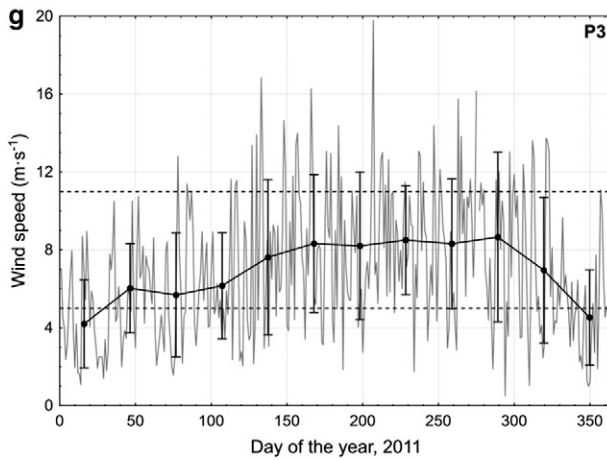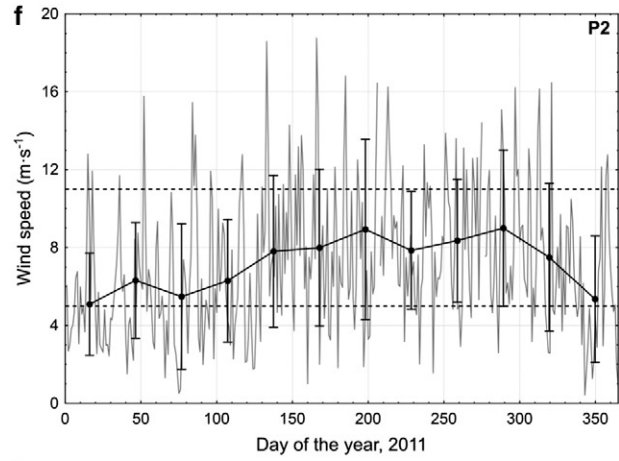

Fig. 2. Overview of the Amundsen Sea region, indicating data cover, location of verification polygons (cross-hatched, from left AOI1, AOI2, AOI3, AOI4) and location of points where meteorological data where studied (P1–P4).
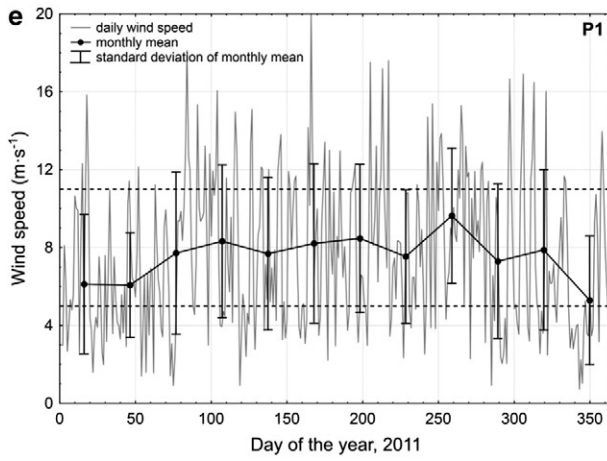
Fig. 4. Comparison between original image and image filtered using Frost Filter with kernel size 3 × 3. The two red contours indicate the border of two icebergs in the unfiltered image and demonstrate the effect of the filter (subsets present zoomed-in version of the right-hand iceberg).

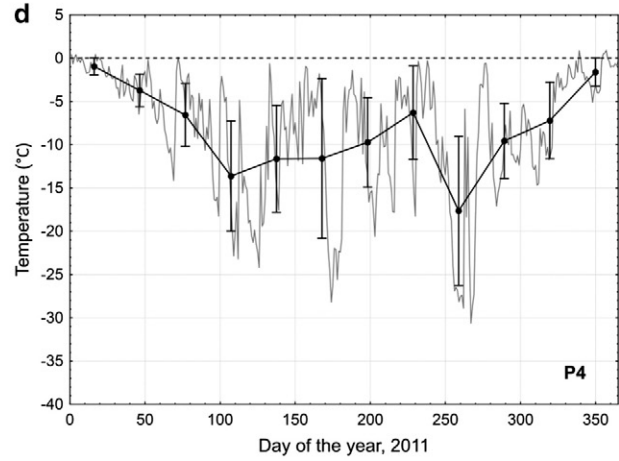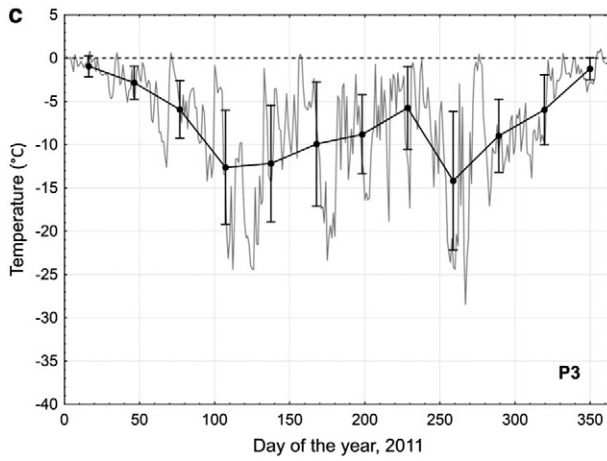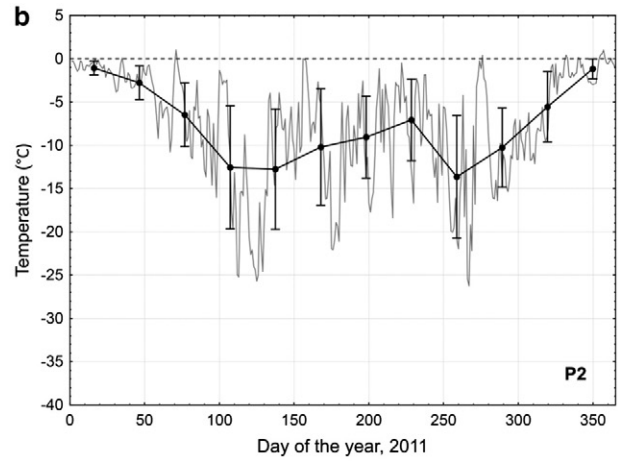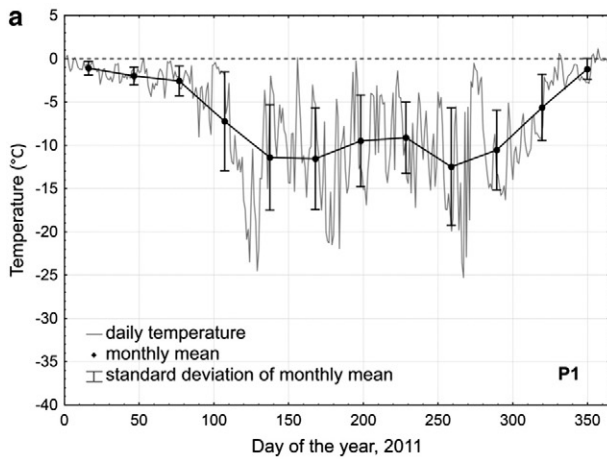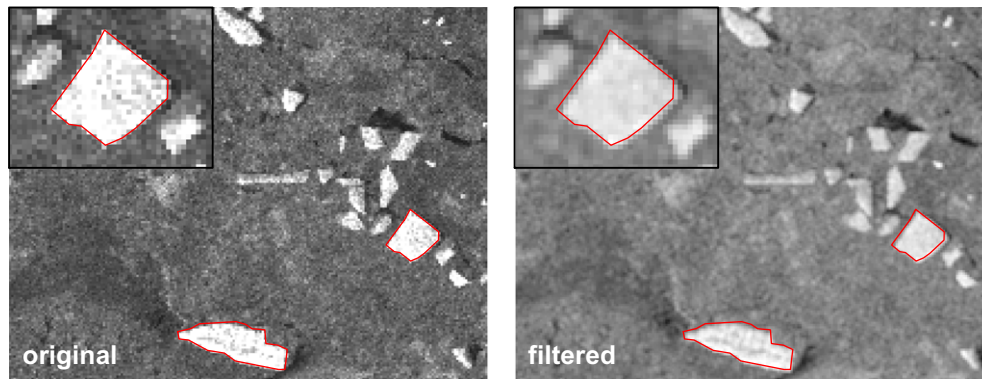calibrated. As a first step all images were georectified to Lambert Azimutal Equal Area projection (central meridian – 115°W and latitude of origin – 90°S) using NEST DAT 5.1 (Next ESA SAR Toolbox, 2015). As the study is focused on the Amundsen Sea a subset (longitude 100°W – 135°W, latitude 70°S – 76°S) was extracted from the original image.

In order to remove radiometric distortions caused by the varying incidence angle the images were calibrated to show the normalized gamma (γ) coefficient according to Rosich and Meadows (2004):

$$\gamma = \frac{DN^2}{K} \frac{sin\alpha}{cos\alpha} \tag{1}$$

where K is the absolute calibration constant, DN^2 is pixel intensity and α is incidence angle.

3.2. Filtration

Speckle noise (the grainy 'salt and pepper' pattern caused by random interference) inherently exists on SAR images, and this disturbance has to be reduced. This can be achieved by multi-looking or spatial filtering. Multi-looking (i.e. summing and averaging single looks) is usually done during signal processing. It reduces speckle but results in a spatial resolution loss (Raney, 1998). The current ASAR WSM data have 11.5 equivalent number of looks at a ground resolution of 150 m (Envisat ASAR Product Handbook, 2007). Additional speckle reduction by spatial filtering was also performed. In order to preserve the edges better the filtering was performed on the square root of γ (Eq. 1).

A good filter for our purposes should reduce speckle while preserving edges between different areas and spatial signal variability. Spatial filters can be either non-adaptive or adaptive. Non-adaptive filters can be based on the mean or the median and use the same set of weights over the entire image. They tend to smooth away details such as edges. Adaptive filters, for example Frost (Frost et al., 1982) and Lee (Lee, 1981) filters accommodate changes in local properties and tend to better preserve edges while removing speckle noise (Mansourpour et al., 2006; Serkan et al., 2008; Wang et al., 2012). For the current data a Frost filter (Frost et al., 1982) with kernel size 3 × 3 was used. The effect of the filter is shown in Fig. 4: It reduces the speckle and makes objects more homogeneous (thereby aiding the segmentation

process) by smoothing of details. However, it also blurs the image and slightly increases the size of objects.

After filtering the data were converted to logarithmical scale (dB) according to:

$$\gamma[dB] = 10 \cdot log_{10}\gamma \tag{2}$$

4. Icebergs detection

In order to improve automatic detection of icebergs in the challenging environmental conditions (i.e. presence of deformed sea ice) an OBIA based detection algorithm was developed. An overview of the identification process is presented in Fig. 5. The SAR image is divided into objects through a segmentation algorithm (Section 4.1). These are then identified as icebergs or non-icebergs (Section 4.2). In order to correctly identify icebergs of all different sizes, a method employing several segmentation levels (corresponding to different size objects), the multi-scale segmentation described in Baatz and Schäpe (2000), was implemented. The method creates a hierarchical network of super- and sub-segments and allows examination of relations between objects at different scale levels. The method was implemented using the eCognition Developer software (eCognition Developer, 2015).

4.1. Segmentation

Fig. 6 shows a sketch of the segmentation process. It starts from single pixels at the bottom level. At each step a pair of objects is merged into a larger segment until the maximum permitted heterogeneity for that level (given by the user-defined scale parameter) is achieved. The merging decision is based on the homogeneity value, which is a combination between the object's shape and how homogeneous its brightness is. The relative importance between shape and brightness is set by the user. The shape parameter is used to prevent segments having frayed borders. More weight on smoothness maintains the ability to produce non-compact data while more weight on compactness gives more round objects. The latter is used when rather compact objects are to be separated from non-compact segments by relatively weak spectral contrast. The relative importance between smoothness and compactness is also set by the user.

Fig. 3. Daily air temperature (a–d) and daily wind speed conditions (e–h) in the four verification points indicated in Fig. 1. The dashed lines show the optimal temperature (below 0 °C) and wind speed values for iceberg detection (below 5 m·s⁻¹ or above 11 m·s⁻¹) (Wesche and Dierking, 2012; Willis et al., 1996).
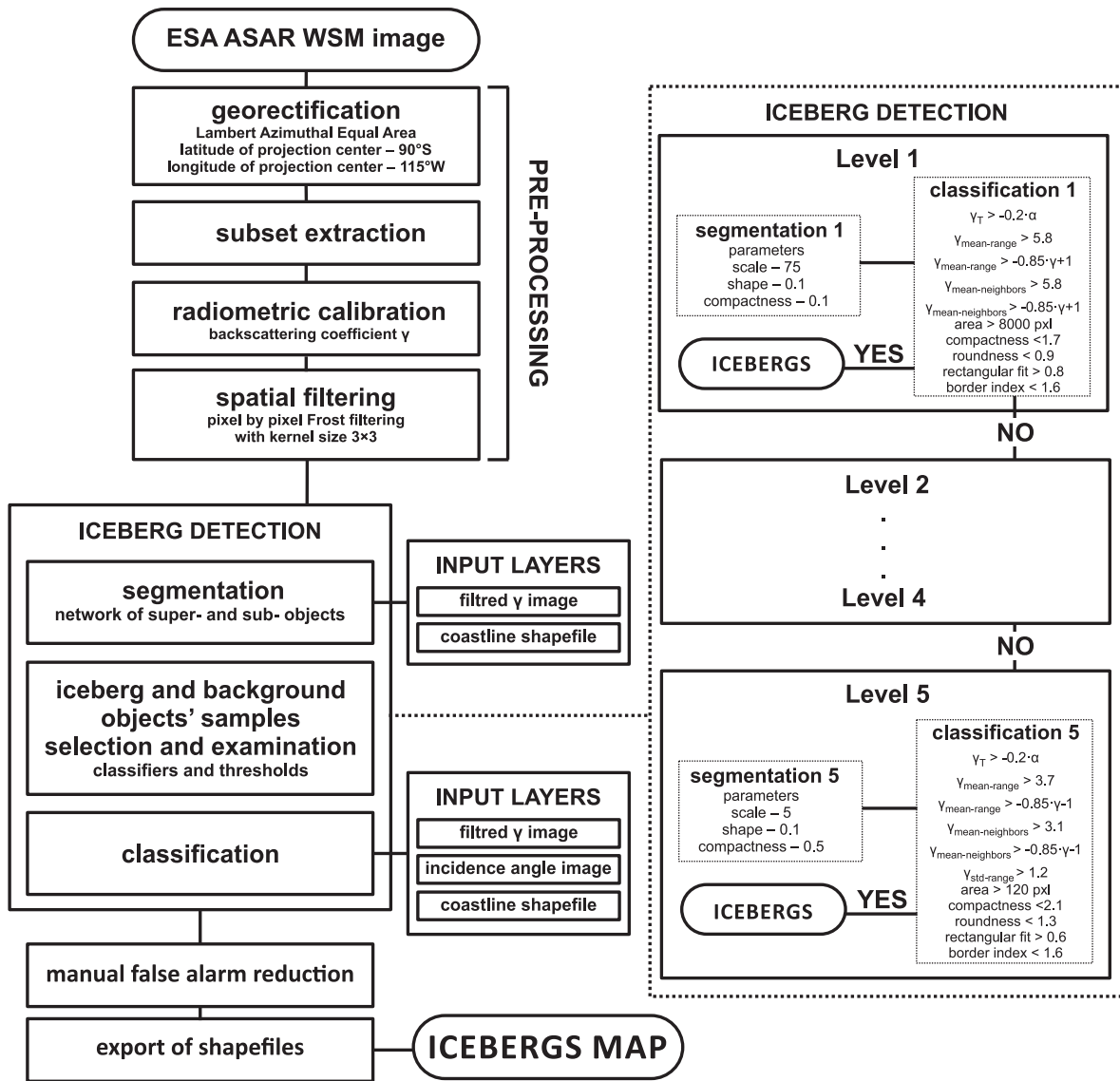
Fig. 5. Flowchart of the object-based iceberg identification process. Dashed rectangle illustrates how the segmentation is performed at the five scale levels, and the parameters used for iceberg classification at each level (see also Table 2).

Merging stops when the homogeneity of the merged object exceeds the value of the scale parameter. A higher scale parameter will hence allow more merging which results in larger objects and vice versa. The process is reversible, i.e. objects can be created by starting from larger segments (at larger scale parameter) and splitting them into the most homogeneous elements possible. Using this method a number of objects are defined at each scale level.
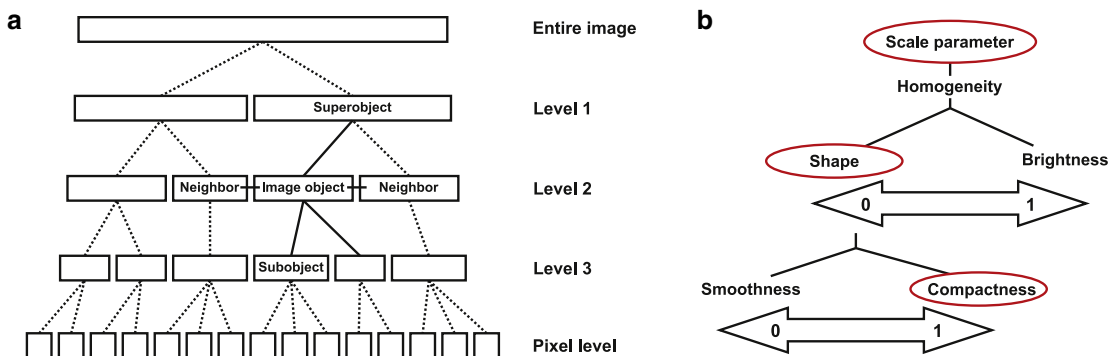

Fig. 6. Network of sub- and super objects created during multiresolution segmentation process (a) and conceptual sketch showing how the homogeneity value is a combination of brightness and shape, and smoothness and compactness (b). Arrows show the relative importance between the two parameters, a value between 0 and 1 that is set by the user (Table 1).

Table 1

Scale parameter and shape and compactness weight parameter settings appropriate for the segmentation process. Level refers to icebergs sizes – the higher level the smaller objects.

Level	Scale parameter	Relative importance of	
		Shape (%)	Compactness(%)
1	75	10	10
2	50	10	10
3	25	10	50
4	10	10	50
5	5	10	50

Table 2

Number of object samples of icebergs and background at different levels.

Level	Number of samples	
	Icebergs	Background
1	35	345
2	47	561
3	189	762
4	491	970
5	457	865
TOTAL	1219	3503

The scale, shape and compactness parameters - needed for automatic segmentation – are shown in Table 1. They were chosen using the Estimation of Scale Parameter 2 (ESP 2) tool (Drăguţ et al., 2014) and based on visual interpretation of segmentation results. Five different object levels were used in order to encompass the different sizes of icebergs present in the area (Fig. 7). The segmentation process was started from creating large objects that were split into smaller segments at the next segmentation stages. The shape weights were set to 0.1. The compactness weights were set to 0.1 for higher scale parameters and 0.5 at the lower levels.

Furthermore a coastline shape file was added in order to block out the continent during the segmentation process.

4.2. Separating icebergs from background objects

The next step is to separate icebergs from the background. As objects' properties differ with scale levels, classifiers and thresholds have to be determined at each level separately. To do this, 12 sample images were selected (recorded on 24 Jan, 16 Feb, 17 Mar, 15 Apr, 15 May, 16 Jun, 16 Jul, 16 Aug, 15 Sep, 16 Oct, 15 Nov and 15 Dec) with different
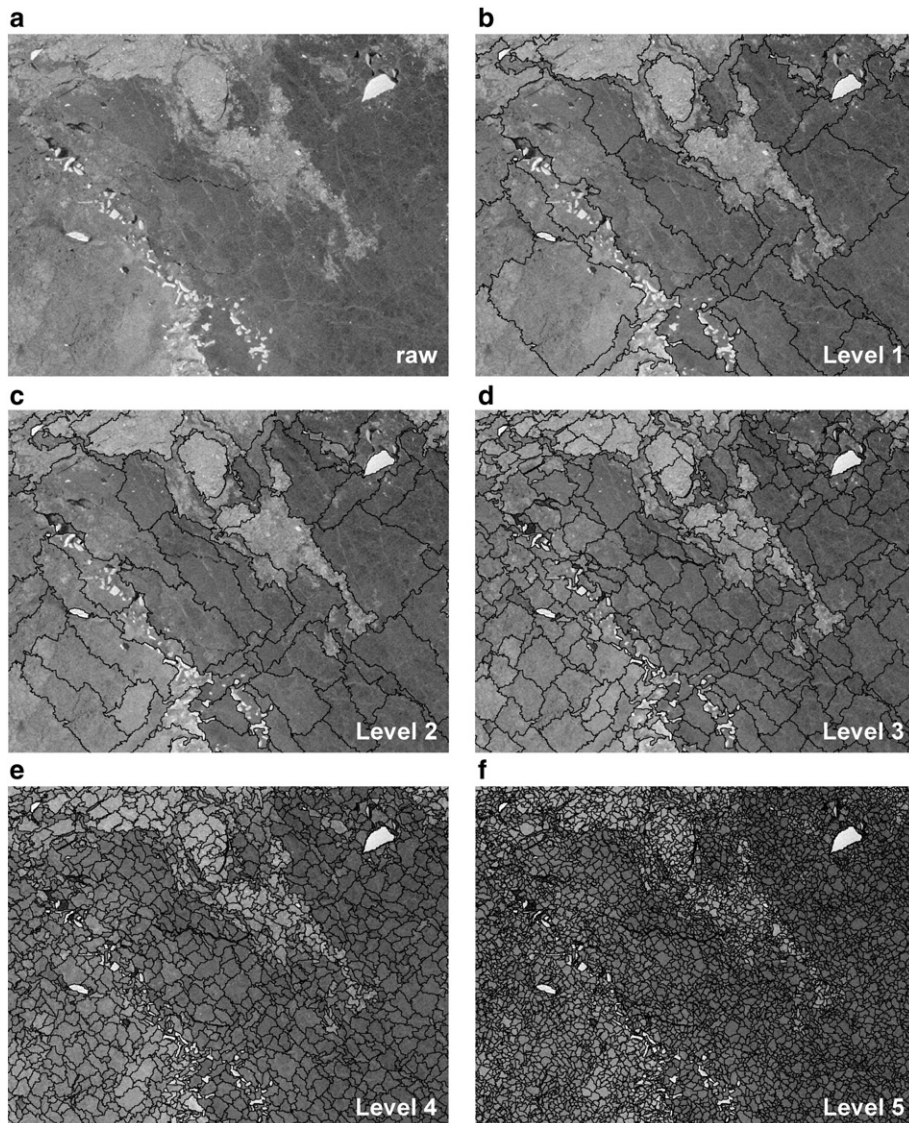

Fig. 7. An example of an original image and segments at different scale levels.

seasons, sea state, sea ice conditions and incidence angle. Through the segmentation algorithm, 4722 objects were obtained. In similarity with the algorithm development in e.g. Wesche and Dierking (2012); Williams et al. (1999); Willis et al. (1996); Young et al. (1998) these were visually inspected and classified into 1219 iceberg objects and 3503 background objects (Table 2).

Fig. 8 shows the icebergs (blue triangles) and background (black dots) objects as a function of γ (Eq. 2) and incidence angle. As can be seen, even though γ is normalized with incidence angle the distinction between icebergs and background still vary with the angle. The empirically best linear fit of the threshold γ_T as a function of incidence angle (α) is given by:

$$\gamma_T = -0.2 \cdot \alpha \tag{3}$$
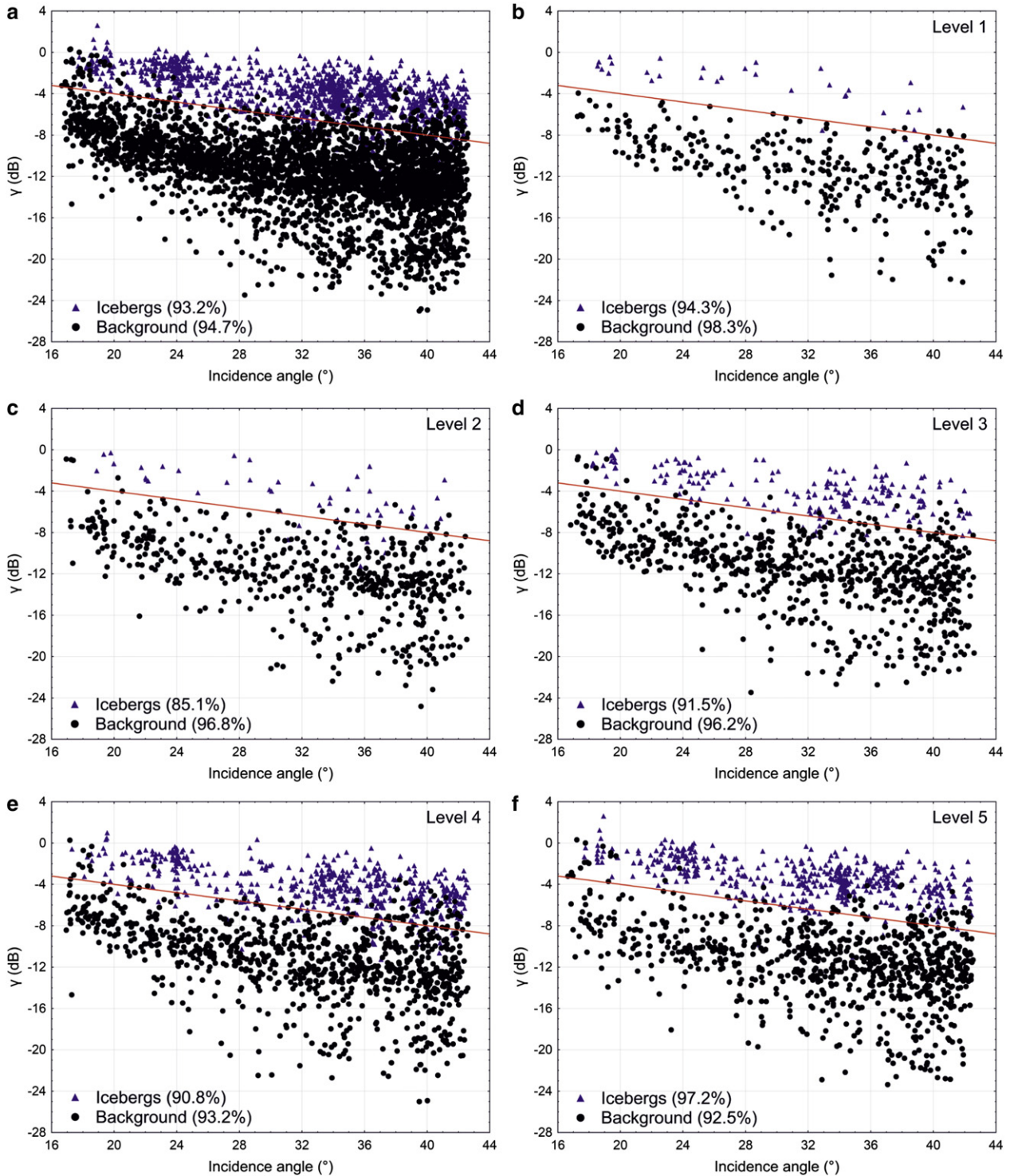

Fig. 8. Result of the manually classified sample images (purple is icebergs, black is background) together with the best linear fit (Eq. 3) for the distinction between icebergs and the surroundings (red line) for all samples (a), level 1 (b), level 2 (c), level 3 (d), level 4 (e), level 5 (f). The values in parentheses show the automatic detection performance based on the linear fit.

Fig. 8 shows that over 90% of the objects in the test images were classified correctly using Eq. 3. Misclassifications occur mainly at the near and far range of the image and they are mostly background objects classified as icebergs ('false alarms'). There are also some iceberg objects classified as background ('misses'), especially at level 2.

In order to improve the automatic classification further, two contrast parameters were created: the $\gamma\_mean\text{-}range$ and the $\gamma\_mean\text{-}neighbors$. The $\gamma\_mean\text{-}range$ is the difference between γ of an object and the mean γ of objects within 50 pixels from it. The $\gamma\_mean\text{-}neighbors$ is the difference between γ of an object and the mean γ for neighbor objects (i.e. which share border). In general, the higher the values of the

$\gamma\_mean\text{-}range$ and the $\gamma\_mean\text{-}neighbors$ are, the higher the contrast between an analyzed segment and its surroundings. Fig. 9 shows the relationship between the $\gamma\_mean\text{-} range$ parameter and γ at different scale levels while the relationship between the $\gamma\_mean\text{-}neighbors$ parameter and γ is presented in Fig. 10. In both cases iceberg and background create two separate point clouds. The best empirically set linear fits (red lines in Figs. 9 and 10) to distinguish both collections at different scale levels are presented in Table 3. The correct distinction rate was high, on average 95%. However misclassifications, particularly amongst the samples of low contrast and high γ value can be seen. In order to reduce misclassifications an additional criterion based on the

Fig. 9. Relationship between γ (dB) and the $\gamma\_mean\text{-}range$ (dB) for all samples (a), level 1 (b), level 2 (c), level 3 (d), level 4 (e), level 5 (f). The red straight line is the best linear fit for the distinction between icebergs and the surroundings. The values in parentheses show the detection performance based on this threshold. The purple line is the value of the γ mean-range parameter threshold.
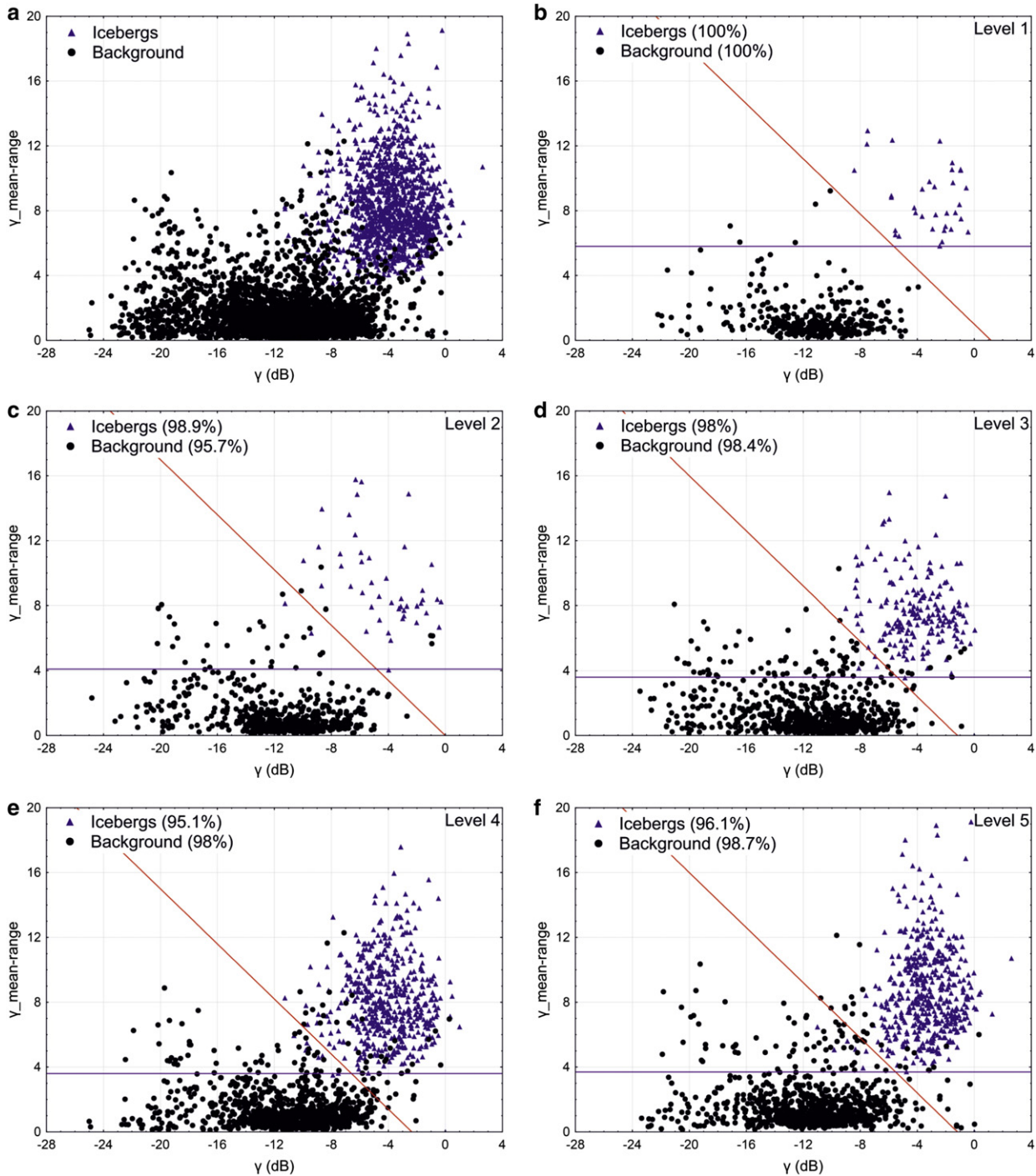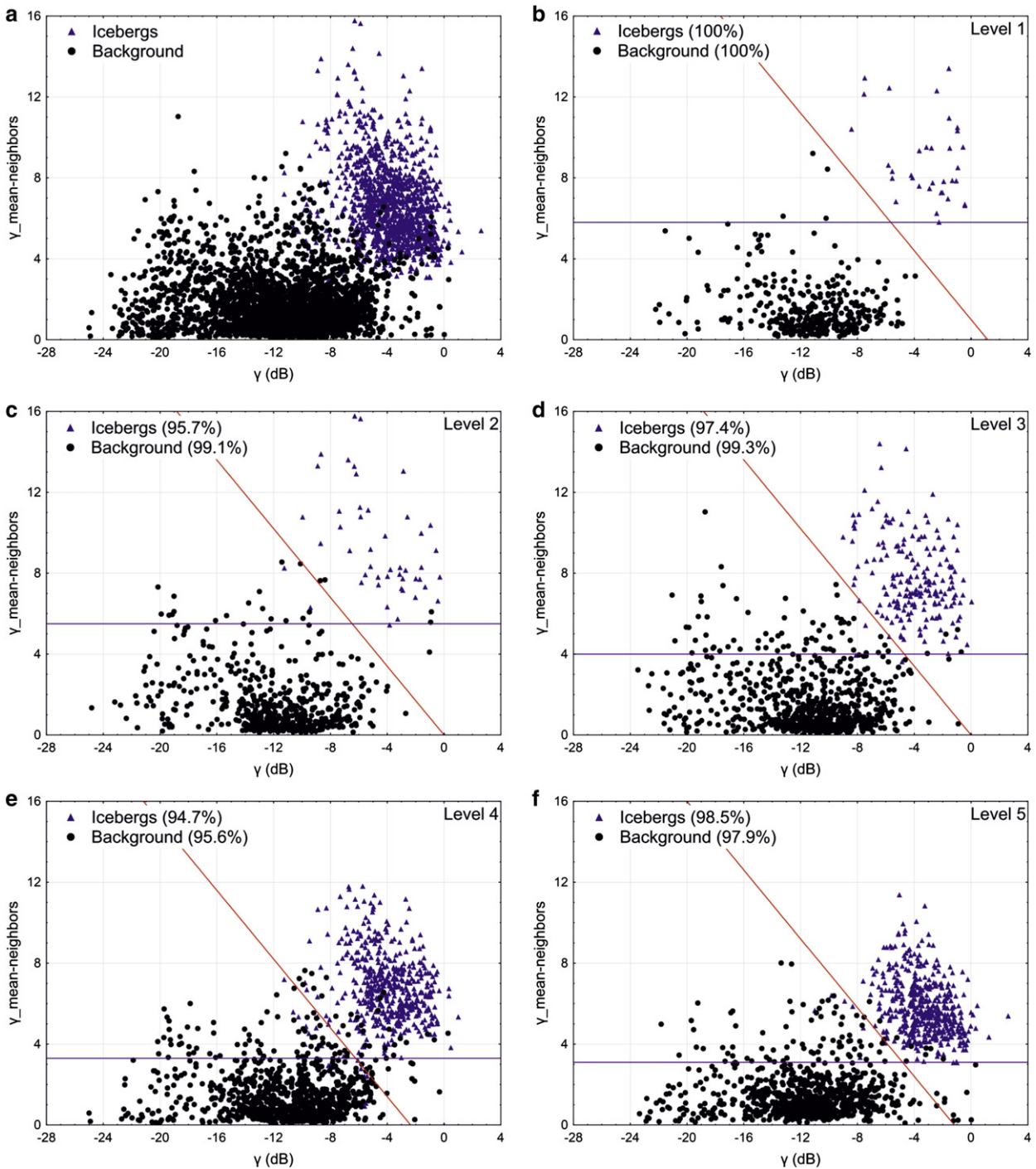
Fig. 10. Relationship between γ (dB) and the γ_mean-neighbors (dB) for all samples (a), level 1 (b), level 2 (c), level 3 (d), level 4 (e), level 5 (f). The red straight line is the best linear fit for the distinction between icebergs and the surroundings. The values in parentheses show the detection performance based on this threshold. The purple line is the value of the γ_mean-neighbors parameter threshold.

minimum γ_mean-range and γ mean-neighbors value classified as icebergs was added (Figs. 9 and 10, purple lines).

According to the contrast parameters (Figs. 9 and 10), iceberg objects should be the brightest segments amongst their neighbors. However, sea ice in a late stage of development can sometimes be brighter than the icebergs. Hence, a contrast and homogeneity based parameter – the γ_std-range – was created that quantifies the homogeneity of the iceberg. The γ_std-range is the difference between the standard deviation of an object's γ and the standard deviation of γ for objects within 50 pixels from it. This parameter makes it easier to distinguish icebergs when they are surrounded by sea ice floes, as icebergs are usually more

homogenous. The higher the value of the γ_std-range parameter, the more homogeneous the segment is compared to the surroundings. The determined thresholds of the γ_std-range parameter are presented in Table 3 for different scale levels. Sea ice floes have a typical size that appears at levels 3, 4 and 5 and the γ_std-range threshold was added at those scale levels.

In order to improve the algorithm even further spatial features of the objects were also included. Icebergs are usually more compact and have less frayed borders compared to background segments. Even though spatial features cannot be used alone to separate icebergs from background, it can be used to improve the results based on the γ and contrast

Table 3
The γ_mean-range, the γ_mean-neighbors and the γ_std-range thresholds as a value and as a function of γ at different scale levels.

	γ_mean-range		γ_mean-neighbors		γ_std-range
Level 1	>5.8	$-0.85 \cdot \gamma + 1$	>5.8	$-0.85 \cdot \gamma + 1$	–
Level 2	>4.1	$-0.85 \cdot \gamma$	>5.5	$-0.85 \cdot \gamma$	–
Level 3	>3.6	$-0.85 \cdot \gamma - 1$	>4.0	$-0.85 \cdot \gamma$	>2.5
Level 4	>3.6	$-0.85 \cdot \gamma - 2$	>3.3	$-0.85 \cdot \gamma - 2$	>1.7
Level 5	>3.7	$-0.85 \cdot \gamma - 1$	>3.1	$-0.85 \cdot \gamma - 1$	>1.2

criteria. The spatial parameters considered here were: area, border index, compactness and roundness or rectangular fit (Table 4). The area is given by the number of pixels forming an object. The border index and compactness parameters describe the smoothness of an object. The border index is calculated as the ratio of the border length of the object and the border length of its smallest enclosing rectangle. Compactness is calculated as the product of the object's length and width divided by its area. In both cases the value 1 describes a smooth segment without any frayed borders. The roundness and the rectangular fit parameters are used to describe the shape. The roundness is calculated as the ratio between the radius of the smallest enclosing ellipse and the radius of the largest enclosed ellipse of the object. The rectangular fit is based on the rectangle with the same area as the considered object and compares the area of the object outside this rectangle with the empty area inside the rectangle. In general the lower roundness value the more round an object is and the closer to the value 1 the rectangular fit parameter is the more square a segment is. During the classification process round and rectangular icebergs were analyzed separately. A more detailed description of all spatial parameters is available in the eCognition Developer reference book (Trimble Documentation, 2014). Similarly to the γ value based parameters the thresholds were determined based on sample analysis and set to the minimum or maximum values observed amongst all iceberg samples at each scale level (Table 4).

Fig. 11 shows the result for all the samples after applying all above mentioned parameters and thresholds. As can be seen there is a certain overlap in the parameter values between icebergs and background which results in icebergs not distinguished or background objects mistakenly classified as icebergs (see e.g. Wesche and Dierking, 2012).

The classification accuracy based on mean segment brightness only is about 94.3%. After implementing contrast and shape parameters the overall accuracy increased to 97.4%. There is a small increase in number of misses after applying contrast and shape parameters particularly in summer and autumn where sea ice floes characteristics are very similar to icebergs properties. This is due to the inherent trade-off between detection rate and false alarm rate. False alarms (e.g. present on the left side of the plot) are caused by high backscatter for water under near incidence angles or free-flowing, deformed sea ice floes with high brightness. The former were partially corrected by use of the spatial parameters (orange dots). Missed icebergs (e.g. present on the right side of the plot) are caused by low brightness contrast between icebergs and surroundings (sea ice in late stage of development). The thresholds were set to reduce the false alarm rate during summer and autumn, and the average false alarm rate was <1% of all objects after implementing contrast and shape parameters in the classification. The highest level

Table 4
The threshold values of spatial parameters at different scale levels set in the iceberg classification process.

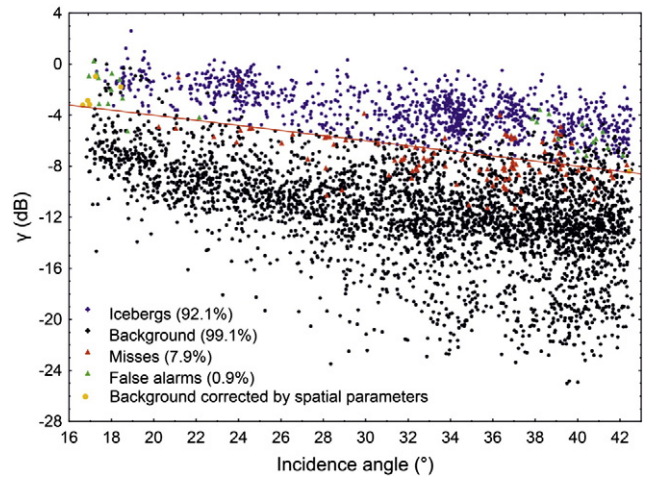| Parameter	Level 1	Level 2	Level 3	Level 4	Level 5
Area	<8000	<7000	<950	<500	<120
Compactness	<1.7	<2.3	<2.7	<3.7	<2.1
Roundness	<0.9	<1.4	<1.9	<2.1	<1.3
Rectangular fit	>0.8	>0.6	>0.5	>0.4	>0.6
Border index	<1.6	<1.7	<2.1	<2.1	<1.6

Fig. 11. Classification result of all object samples based on defined parameters and thresholds. The red line is the best linear fit for the distinction between icebergs and the surroundings based on the object brightness value (see Fig. 8a). Purple and black dots are correctly classified icebergs and the background, respectively. Red triangles represent missed icebergs, green triangles are false alarms. Orange dots are background objects classified as icebergs by parameters based on the brightness value but corrected with the use of spatial parameters.

of both misses and false alarms were observed at scale level 4, the size of many sea ice floes formed in the Amundsen Sea.

5. Results and validation

Using the results from the previous section, classification of created objects was performed on SAR data collected over the Amundsen Sea during 2011. The largest objects were created at level 1 and classified into icebergs and background based on the thresholds determined during analysis of samples at this level (Table 3–4). Next, the image was segmented again creating level 2, leaving out objects classified as icebergs in the previous classification. Classification of icebergs was then again carried out based on thresholds corresponding to level 2 (Table 3–4). In a similar fashion segmentation and classification was conducted at the three remaining levels. The segmentation and classification process depends on the image size and takes between 5 and 15 min on an Intel Core I7 CPU workstation with 16 GB of memory. An example of the result is shown in Fig. 12.

After visual inspection (with detection of missed icebergs and false alarm reduction) the iceberg segments were exported as a shape file.

In order to validate the classification results we used Level-1B imagery taken from the Digital Mapping System (DMS) over the Amundsen Sea during NASA's Operation IceBridge mission in 2011 (Dominguez, 2010). In general iceberg detection on radar data depends on many factors and is not directly limited by the pixel size. However, there were 12 icebergs which were detected on IceBridge images and were smaller than 150 m along both axes (width and length), none of which could be seen on ASAR images. If at least one dimension is larger that the pixel size (150 m) an echo signal might be high enough that an iceberg can be detected on ASAR data; there were 29 such icebergs identified in IceBridge data that overlapped in time and space with ASAR acquisitions (e.g. Fig. 13).

Comparing the two data sets, 16 icebergs out of 29 could be detected and were correctly identified on overlapping IceBridge and ASAR images. Undetectable icebergs, i.e. icebergs present on IceBridge images and not seen on overlapping ASAR images occured in 11 cases, and 9 icebergs out of these 11 were larger that the pixel size (150 m) in one dimension. Two icebergs out of 18 detectable were missed in the automatic detection process but could be detected manually on the ASAR
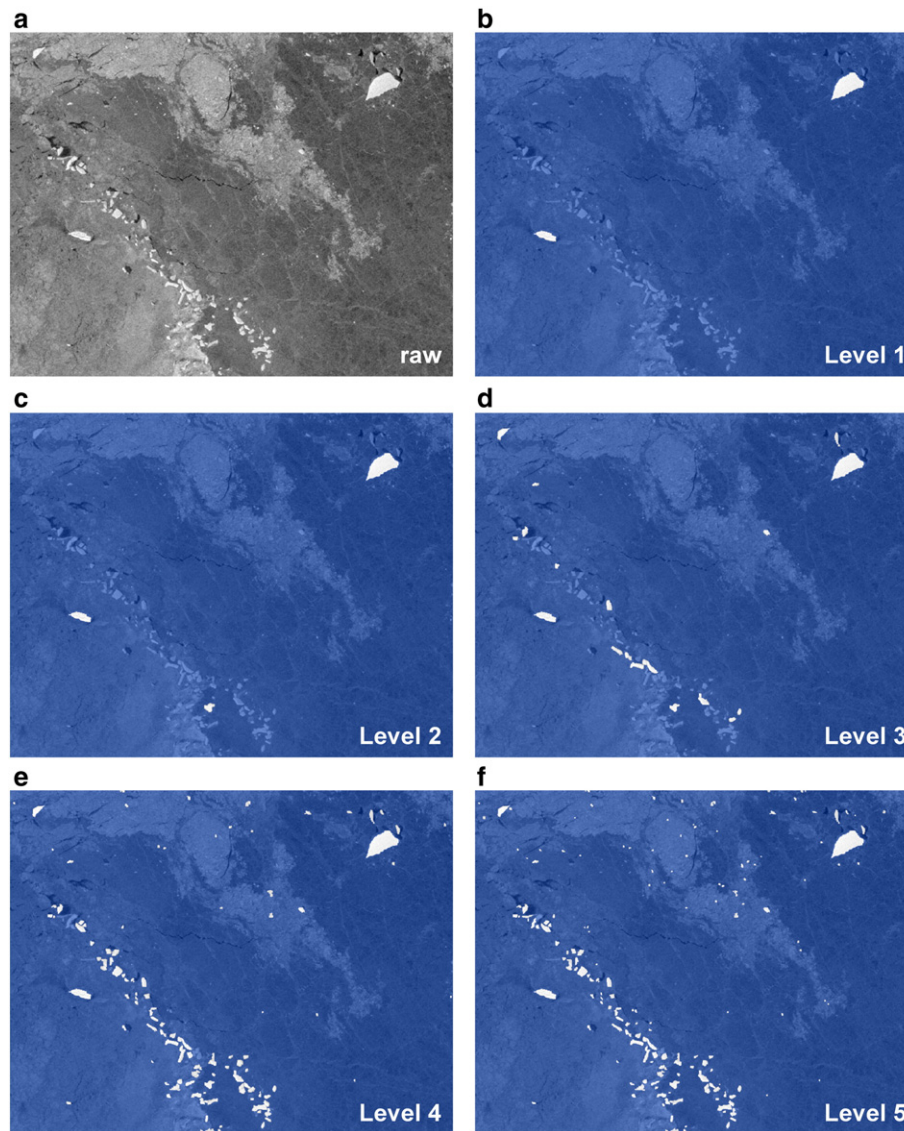
Fig. 12. An example of an original image and classification results at different scale levels (before visual inspection). Blue color indicates no icebergs detected, white areas indicate detected icebergs.

images. It was also noted that icebergs closer than 150 m apart were not separated in the segmentation process as single segments. As a result clusters of icebergs were merged into one object (eg. Fig. 13, lower subset).

In general it is difficult to distinguish icebergs from sea ice floes on Landsat imagery, which is also affected by stripes on large portions of the image caused by the failure of the scan line corrector (see e.g. Fig. 1). Hence Landsat imagery could not be used for validation of the algorithm. However by picking icebergs from SAR images and locating them on corresponding Landsat images we could compare the size estimate from radar and optical data. This was done by manually digitizing bergs present on IceBridge and Landsat data (e.g. Fig. 1 left), calculating the area and comparing it with the classification results (Fig. 14). As expected, larger icebergs had smaller relative error in the size estimate. For icebergs larger than 5 km^2 the error was around ±5%, and for icebergs with an area larger than 50 km^2 the error was around ±1%. Higher relative size errors, even up to ±100% for the smallest ones having an area comparable to the pixel size, were observed for smaller icebergs (Fig. 14).

Since available iceberg observations from independent sources such as Landsat and IceBridge are very limited, further examination of the algorithm performance is done based on manually classified icebergs in the ASAR images (in similarity with e.g. Silva and Bigg, 2005; Wesche and Dierking, 2015; Williams et al., 1999). For that purpose four verification areas (90 × 90 km) were selected (Fig. 2). These areas represent specific regions: (i) where icebergs tend to drift together with sea ice (AOI 1 and AOI 4), (ii) where icebergs accumulate but high sea ice drift is present (AOI 2), (iii) where icebergs often accumulate and there is little sea ice drift present (AOI 3). The images for verification were randomly chosen from all four seasons, avoiding the images used to calibrate the algorithm (Table 2). A comparison between automatic (using the criterion in Tables 3–4) and manual detection for different areas and seasons is presented in Table 5. The comparison was made before the manual reclassification of misses and false alarms was undertaken.

Additionally in each verification area Cohen's Kappa coefficient (κ), comparing the observed accuracy with the expected, was calculated (Cohen, 1960) (Table 6). When there is no agreement other than that which would be expected by chance κ is zero. When there is total agreement, κ is one.

Based on Table 6 the worst classification results were obtained in spring in AOI 1 and in autumn in AOI 4 (Fig. 15), during wind-roughened water (Fig. 15a) and presence of sea ice floes (Fig. 15b).
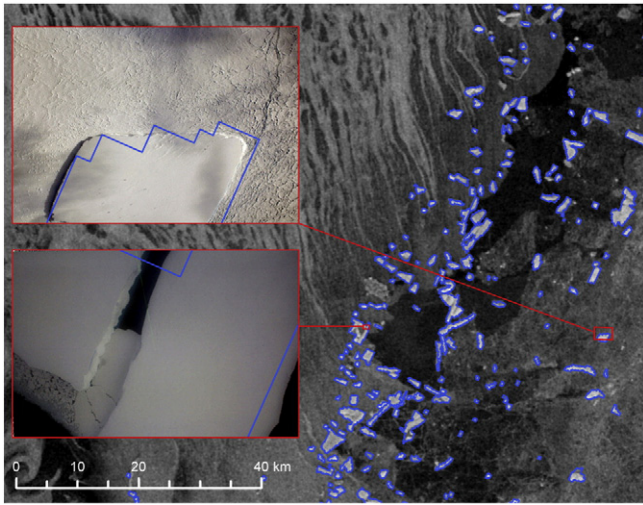
Fig. 13. An example of IceBridge aerial photographs taken on 17th Oct 2011 (subsets) and an ASAR image taken on 18th Oct 2011 (background). The blue lines indicate the classification result compared with an ASAR data and a high resolution aerial image.
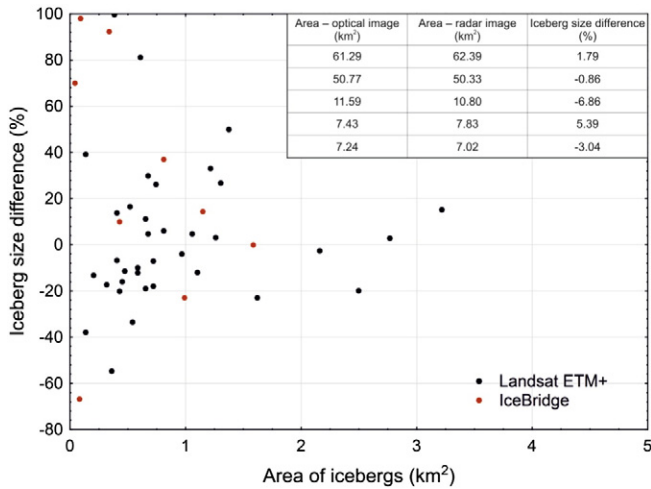

Fig. 14. Comparison between icebergs sizes estimated from ASAR images and from Landsat (black) and IceBridge (red) images. Values in the table are derived from Landsat images.

Table 6
The Kappa coefficient (κ) calculated in different verification areas.

Area	Summer	Autumn	Winter	Spring
AOI 1	0.973	0.892	0.964	0.569
AOI 2	0.992	0.891	0.960	0.885
AOI 3	0.879	0.906	0.857	0.923
AOI 4	0.809	0.224	0.892	0.839

Although the majority of the icebergs present in those polygons were detected, false alarms were also observed. Sea ice-induced mis-classification (mainly during summer and autumn) was more common than wind-induced misclassification. Wind-induced misclassification occurred on a few images only, and it was limited to the near range of the radar scene. For wind-induced misclassification all icebergs were classified but the false alarm rate was 28.6% of the number of icebergs (i.e. the algorithm detected 28.6% more icebergs than present in the area), which corresponded to an iceberg area overstimation of 1.5 times (Table 5). This accounted for 0.15% of the total area. Table 7 shows iceberg classification results as a function of size and season for the four AOI's. Icebergs smaller than 1 km^2 had an average detection rate of 96.9%, while icebergs larger than 1 km^2 had lower detection rate of 95.4%. The average was 96.2%, which corresponds to 93.2% of the iceberg area. One of the worst classification results is shown in Fig. 15b, where false alarms led to a doubling of the number of icebergs and a large overstimation of the iceberg area. However, such high false alarm rate (0.75% of the total polygon area) were observed on only about 5% of the images and in certain parts of the Amundsen Sea. The the overall false alarm rate for all verification polygons was 7.0% (16.8% based on the iceberg area) and the overall rate of misses was 3.8% (6.8% based on the iceberg area) (Table 5). The highest number of missed icebergs were observed in AOI 3 – where icebergs accumulate. Misclassifications appear to be caused by icebergs frozen together or being very close. Icebergs which are within 1 pixel distance are rarely separated during the segmentation process. Also large icebergs, if not sufficiently homogeneous, may be under segmented. However, it is straight forward to resegment and reclassify such areas during the manual misses and false alarm reduction.

As an application and output of the new algorithm, a probability map has been constructed (Fig. 16). The colors indicate the probability of finding an iceberg inside a grid cell (7.5×7.5 km), calculated by division of the number of days that an iceberg is found by the number of days that have SAR image coverage. As expected there is a high probability of finding icebergs on top of shallow ridges and banks, with probability curves coinciding with depth contours in areas close to the main iceberg sources (i.e. the ice shelf fronts). The fact that the bathymetric data so

Table 5
Comparison between automatic and manual detection of icebergs in different seasons of 2011. AOI 1 indicates area of interest 1, etc. (Fig. 2).

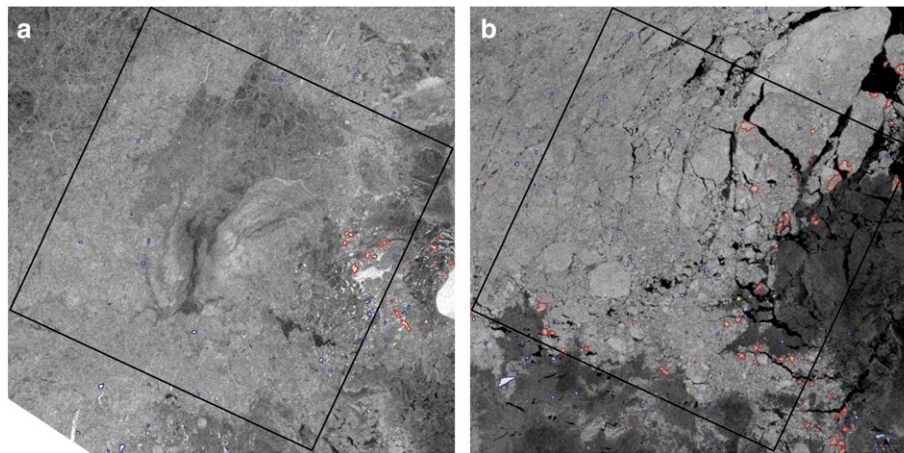| AOI		Summer		Autumn		Winter		Spring	
		Number of icebergs	Area of icebergs (km^2)	Number of icebergs	Area of icebergs (km^2)	Number of icebergs	Area of icebergs (km^2)	Number of icebergs	Area of icebergs (km^2)
1	Correct	7	3.2	52	22.6	30	42.5	21	7.8
	Miss	0	0.0	7	3.6	0	0.0	0	0.0
	False alarms	1	0.2	8	1.8	2	3.1	6	11.8
2	Correct	41	129.7	64	94.2	93	133.6	63	94.2
	Miss	0	0.0	1	0.6	2	2.2	1	1.9
	False alarms	2	2.2	1	22.1	4	8.7	3	22.1
3	Correct	145	218.9	166	249.6	150	228.0	149	236.9
	Miss	10	31.4	5	19.9	5	32.3	4	9.9
	False alarms	4	26.6	2	29.9	5	40.8	5	28.6
4	Correct	4	2.7	28	8.9	99	47.4	33	18.3
	Miss	3	1.3	4	1.6	1	0.4	0	0.0
	False alarms	0	0.0	33	59.4	6	11.1	1	7.0

Fig. 15. Example of classification errors: false alarms due to presence of wind-roughened water in AOI 1 during spring (a) and false alarms caused by presence of deformed sea ice in AOI 4 during autumn (b). Blue color indicates detected icebergs, red and green are false alarms and misses, respectively.

closely coincides with the iceberg probability lends further support to the reliabiity of the method. It can be noted that the high probability of icebergs is centered on the eastward side of ridges, indicating a westward drift of the bergs throughout the whole region.

6. Discussion

An object-based algorithm for iceberg detection, implemented for the Amundsen Sea, has been presented. This is the first time that an iceberg detection algorithm has been applied and verified in the Amundsen Sea for all seasons. The only previous study implemented to this region before was the work by Wesche and Dierking (2015), a pixel-based algorithm based on data aquired during September–October 1997.

In general the current method was shown to work well under atmospheric and oceanographic conditions often prevailing in the Amundsen Sea, i.e. cold temperatures and hard winds. The (limited) available independent validation data (aerial images from operation IceBridge, Dominguez, 2010) show that as expected icebergs smaller than the pixel size (150 m) along both axes are in general not visible on ASAR images. However, the icebergs that were sufficiently large to be detected on ASAR images were shown on their positions and with no false alarms and only few misses as compared to IceBridge data. It would be desirable to in the future have better validation of ASAR detection of icebergs for example by increased optical data gathering or GPS tracking of icebergs.

Error estimates of the iceberg size were also conducted comparing IceBridge and Landsat data to the results of the automatic ASAR classification. In general both positive and negative deviations in iceberg areas were observed and the average error was $\pm 25\%$. This can be compared to the algorithm presented by Wesche and Dierking (2012) which tended to overestimate the area by $10 \pm 21\%$ and to Williams et al. (1999) and Young et al. (1998) that overestimated the area by 20%. In general icebergs smaller than 0.5 km^2 differed by $\pm 48\%$, icebergs

between 0.5 and 1 km^2 differed by $\pm 20\%$, icebergs between 1 and 5 km^2 differed by 13% and icebergs larger than 5 km^2 differed by about $\pm 3\%$. The highest relative errors, up to $\pm 100\%$, were obtained for the smaller icebergs that were comparable in size to ASAR pixels. This is a limitation of the available medium resolution data source and this uncertainty has to be considered in future studies concerning iceberg mass budgets and trends in the Amundsen Sea.

Validation of the algorithm itself was performed by comparing manually detected icebergs in the ASAR images to the automatic classification results in four areas of interest (Fig. 2), in similarity with e.g. Silva and Bigg (2005); Wesche and Dierking (2015) and Williams et al. (1999). The presented algorithm has an average detection rate of 96.2% (corresponding to an area of 93.2%) in the Amundsen Sea. This can be compared to the one presented by Wesche and Dierking (2015) that detected on average 46% (corresponding to an area of 86.7%), the one by Williams et al. (1999) (detecting 84%) and Silva and Bigg (2005) (detecting 70%, corresponding to 70% of the area). In the present study ASAR WSM data with pixel size 150 m × 150 m were used, while Wesche and Dierking (2015) used Radarsat-1 Antarctic Mapping Project mosaic and both Williams et al. (1999) and Silva and Bigg (2005) used ERS-1 images. Both Wesche and Dierking (2015) and Williams et al. (1999) used SAR data with spatial resolution of 100 m × 100 m. The results of Silva and Bigg (2005) were based on SAR images with a pixel size 25 m × 25 m. It should also be pointed out that the present study applies to radar images recorded for the whole year, while previous studies only used winter images.

Although the proposed algorithm shows noteworthy improvement compared to existing methods, false alarms still appear in particular in areas where wind-roughened open water or highly deformed sea ice floes are present (spring AOI 1 or autumn AOI 4; Table 6). The backscatter coefficient of such sea ice floes overlaps with that of icebergs, and they also tend to form quite compact objects with high contrast to the surrounding water. Such sea ice conditions require high user intervention. Excluding these cases the presented algorithm had an average

Table 7
The percentage rate of correctly classified number and area of icebergs of different sizes in different seasons of 2011.

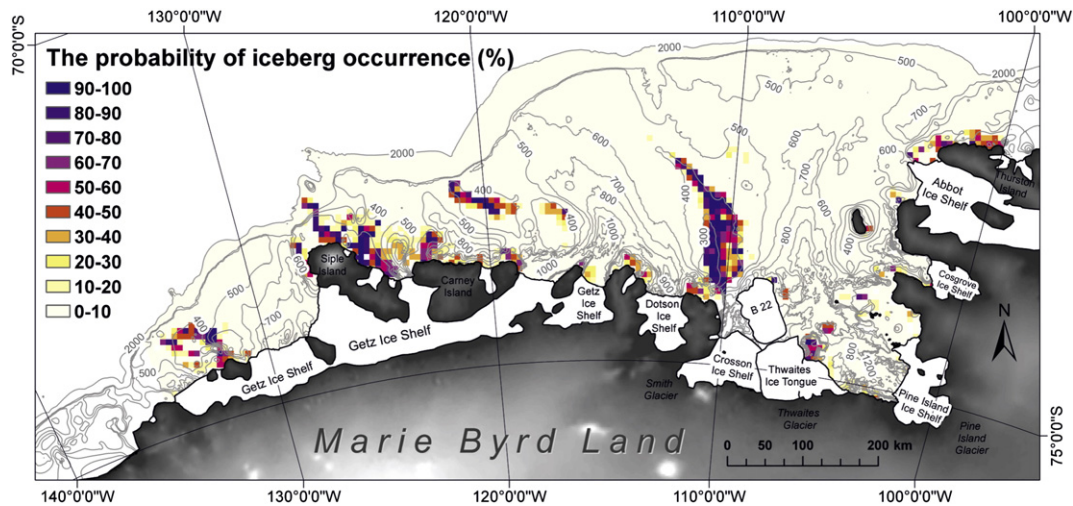| Icebergs area (km2)	Summer Number of icebergs (%)	Area of icebergs (%)	Autumn Number of icebergs (%)	Area of icebergs (%)	Winter Number of icebergs (%)	Area of icebergs (%)	Spring Number of icebergs (%)	Area of icebergs (%)
<0.5	96.0	95.5	94.0	93.0	99.4	99.2	100	100
0.5–1.0	90.8	90.5	96.2	96.0	98.9	98.5	98.5	98.3
1.0–5.0	96.3	97.7	96.1	95.3	96.8	92.6	95.9	94.5
>5	85.7	84.8	85.7	86.9	84.6	88.2	100	100
Net:	93.8	91.6	95	93.6	97.9	92.8	98.2	96.8

Fig. 16. Probability of icebergs occurrence in the Amundsen Sea in 2011. Thin lines indicate bathymetry according to the IBCSO database (Arndt et al., 2013) colors indicate iceberg probability according to the color map.

false alarm rate of 3.9% (based on total number of detected icebergs), which corresponds to an area of 12.6%. The false alarm area accounted for 0.27% of the total verification area. Including the worst scenarios the average false alarm rate based on iceberg number was 7.0%, overestimating the total iceberg area by 16.8% (i.e. 0.29% of the total verification area). This can be compared with the algorithm presented by Williams et al. (1999) generating around 38% of false alarms based on iceberg number and with the method of Silva and Bigg (2005) which overestimated the iceberg area by 30%.

The dependency of the performance of the algorithm on iceberg size (Table 7) is inverse compared to most previous studies. Silva and Bigg (2005), Wesche and Dierking (2015) and Williams et al. (1999) all had increased detectability for larger icebergs (larger than 1 km^2), while the present algorithm had better detection rate for the smallest icebergs. Hence the present algorithm is well suited for the Amundsen Sea where icebergs smaller than 1 km^2 represent around 60% of the population. The reason that the present algorithm better classifies smaller icebergs might be the use of objects, together with parameters which consider relationships between neighbor segments (Table 3–4, Figs. 9 and 10). Small icebergs are in most cases single objects surrounded by water or sea ice and will be well separated by such an algorithm. The method used in this study also separates icebergs from sea ice even with only slightly lower γ values, which is often observed during summer months. The reason for the lower detection rate for larger icebergs (1–5 km^2) appears to be that they get stranded and accumulate, posing difficulties for the algorithm. The present data set only had a small number of very large icebergs (>10 nautical miles along at least one axis) on which the thresholds were based (Table 3–4), and improving the method for very large icebergs is a subject for future work involving even larger datasets.

The performance of the present algorithm is at a similar level during all seasons (except AOI 4 in spring and AOI 1 in autumn) and it tends to generate similar amount of false alarms and misses (3.9% and 3.8%, respectively). The classification accuracy is, in common with other algorithms (Silva and Bigg, 2005; Wesche and Dierking, 2015; Williams et al., 1999; Young et al., 1998), improved by manual inspection and removal of false alarms from the dataset. It is expected that dual-polarized and higher resolution radar data e.g. provided by the SAR sensor on the SENTINEL-1 satellite might significantly improve the performance in the future and also decrease the error in size estimation, especially for icebergs smaller than 1 km^2.

It is expected that the present method will make it possible to advance the important and in the Amundsen Sea comparatively unexplored fields of iceberg formation, drift, and melting including its

influence on water masses, sea ice formation and ocean circulation. There is also a lack of knowledge of the large-scale surface ocean circulation in the Amundsen Sea, since in situ data are sparse and remote sensing methods often fail due to the sea ice cover.

7. Summary

In this study 432 ASAR WSM images acquired in 2011 were analyzed in order to detect and classify icebergs in the Amundsen Sea, Antarctica. An object-based iceberg classification algorithm was developed and shown to work well under atmospheric and oceanographic conditions prevailing in this region i.e. cold temperatures and hard winds. A spatial filter was designed and applied to the square root of γ (Eq. 2) which reduced speckle but kept the image characteristics needed for the segmentation. Segmentation and classification were carried out hierarchically at different scale levels. Multiresolution segmentation was used in order to avoid under- and over- segmentation. Icebergs were classified based on a set of criteria. One of the best distinguishers was contrast based (γ_mean-range) and detected around 96% of all icebergs. Additional spatial parameters such as area, border index, compactness, roundness and rectangular fit was also included to exclude bright objects with complex shapes such as sea ice filaments. All thresholds were determined based on analysis of a variety of icebergs and background samples.

The results were verified based on IceBridge data as well as manual iceberg detection results in four verification polygons in different seasons. The algorithm was shown to detect 96.2% (corresponding to an iceberg area of 93.2%) of icebergs visible on ASAR images in the Amundsen Sea and the detection rate was aproximately at the same level during all seasons. The performance of the algorithm on iceberg size is inverse compared to most previous studies with improved performance for smaller bergs. It is well suited for the Amundsen Sea where icebergs smaller than 1 km^2 represent around 60% of the population. Further improvement of the algorithm is made by manual correction of misses and false alarms. In general the algorithm tended to generate similar number of false alarms as misses, with the majority of the false alarms observed in regions with heavy sea ice drift during in summer and spring. Further validation was given in the form of an iceberg probability map (Fig. 16) which shows that a high probability of icebergs occurrence is associated with topographic ridges. This is also in agreement with Wesche and Dierking (2015) who studied near-coastal iceberg Antarctic iceberg distribution based on the data from 1997.

Although the Amundsen Sea is the most iceberg-productive sea in Antarctica the information on icebergs is sparse (Wesche and Dierking,

2015). This might be because meteorological and oceanographic conditions in the study area are challenging for radar iceberg detection. The presented algorithm appear to detect the vast majority of icebergs under all conditions, with high detection rate of small icebergs common in the Amundsen Sea. As it is believed that the results might be a valuable data source in this area the data have been published in the Pangaea data library (Mazur et al., 2016).

Acknowledgements

References

Arndt, J.E., Schenke, H.W., Jakobsson, M., Nitsche, F.O., Buys, G., Goleby, B., Rebesco, M., Bohoyo, F., Hong, J., Black, J., Greku, R., Udintsev, G., Barrios, F., Reynoso-Peralta, W., Taisei, M., Wigley, R., 2013. The International Bathymetric Chart of the Southern Ocean (IBCSO) version 1.0—a new bathymetric compilation covering circum-Antarctic waters. Geophys. Res. Lett. 40:3111–3117. http://dx.doi.org/10.1002/grl.50413.

Baatz, M., Schäpe, A., 2000. Multiresolution Segmentation: an optimization approach for high quality multi-scale image segmentation. Angewandte Geographische Informationsverarbeitung XII. Wichmann, Heilderberg, pp. 12–23.

Bamber, J.L., Riva, R.E.M., Vermeersen, B.L.A., LeBrocq, A.M., 2009. Reassessment of the potential sea-level rise from a collapse of the west Antarctic ice sheet. Science 324: 901–903. http://dx.doi.org/10.1126/science.1169335.

Beucher, S., Lantuejoul, C., 1978. Use of watersheds in contour detection. Presented at the International Workshop on Image Processing: Real-time Edge and Motion Detection/Estimation. France, Rennes.

Biddle, L.C., Kaiser, J., Heywood, K.J., Thompson, A.F., Jenkins, A., 2015. Ocean glider observations of iceberg-enhanced biological production in the northwestern Weddell Sea. Geophys. Res. Lett. 42:459–465. http://dx.doi.org/10.1002/2014GL062850.

Bintanja, R., van Oldenborgh, G.J., Katsman, C.A., 2015. The effect of increased fresh water from Antarctic ice shelves on future trends in Antarctic sea ice. Ann. Glaciol. 56: 120–126. http://dx.doi.org/10.3189/2015AoG69A001.

Björk, G., Söderkvist, J., Winsor, P., Nikolopoulos, A., Steele, M., 2002. Return of the cold halocline layer to the Amundsen Basin of the Arctic Ocean: implications for the sea ice mass balance. Geophys. Res. Lett. 29:1–8. http://dx.doi.org/10.1029/2001GL014157.

Blaschke, T., 2010. Object based image analysis for remote sensing. ISPRS J. Photogramm. Remote Sens. 65:2–16. http://dx.doi.org/10.1016/j.isprsjprs.2009.06.004.

Blaschke, T., Hay, G.J., Kelly, M., Lang, S., Hofmann, P., Addink, E., Queiroz Feitosa, R., van der Meer, F., van der Werff, H., van Coillie, F., Tiede, D., 2014. Geographic object-based image analysis – towards a new paradigm. ISPRS J. Photogramm. Remote Sens. 87:180–191. http://dx.doi.org/10.1016/j.isprsjprs.2013.09.014.

Bracegirdle, T.J., Marshall, G.J., 2012. The reliability of antarctic tropospheric pressure and temperature in the latest global reanalyses. J. Clim. 25:7138–7146. http://dx.doi.org/10.1175/JCLI-D-11-00685.1.

Carvajal, G.K., Wåhlin, A.K., Eriksson, L.E.B., Ulander, L.M.H., 2013. Correlation between synthetic aperture radar surface winds and deep water velocity in the Amundsen Sea, Antarctica. Remote Sens. 5:4088. http://dx.doi.org/10.3390/rs5084088.

Cleve, C., Kelly, M., Kearns, F.R., Moritz, M., 2008. Classification of the wildland–urban interface: a comparison of pixel- and object-based classifications using high-resolution aerial photography. Comput. Environ. Urban. Syst. 32:317–326. http://dx.doi.org/10.1016/j.compenvurbsys.2007.10.001.

Cohen, J., 1960. A Coefficient of Agreement for Nominal Scales. Educ. Psychol. Meas. 20: 37–46. http://dx.doi.org/10.1177/001316446002000104.

Dee, D.P., Uppala, S.M., Simmons, A.J., Berrisford, P., Poli, P., Kobayashi, S., Andrae, U., Balmaseda, M.A., Balsamo, G., Bauer, P., Bechtold, P., Beljaars, A.C.M., van de Berg, L., Bidlot, J., Bormann, N., Delsol, C., Dragani, R., Fuentes, M., Geer, A.J., Haimberger, L., Healy, S.B., Hersbach, H., Hólm, E.V., Isaksen, L., Kållberg, P., Köhler, M., Matricardi, M., McNally, A.P., Monge-Sanz, B.M., Morcrette, J.-J., Park, B.-K., Peubey, C., de

Rosnay, P., Tavolato, C., Thépaut, J.-N., Vitart, F., 2011. The ERA-Interim reanalysis: configuration and performance of the data assimilation system. Q. J. R. Meteorol. Soc. 137:553–597. http://dx.doi.org/10.1002/qj.828.

Depoorter, M.A., Bamber, J.L., Griggs, J.A., Lenaerts, J.T.M., Ligtenberg, S.R.M., van den Broeke, M.R., Moholdt, G., 2013. Calving fluxes and basal melt rates of Antarctic ice shelves. Nature 502, 89–92.

Dominguez, R., 2010. IceBridge DMS L1B Geolocated and Orthorectified Images. NASA National Snow and Ice Data Center Distributed Active Archive Center, Boulder, Colorado USA.

Drăguţ, L., Csillik, O., Eisank, C., Tiede, D., 2014. Automated parameterisation for multi-scale image segmentation on multiple layers. ISPRS J. Photogramm. Remote Sens. 88:119–127. http://dx.doi.org/10.1016/j.isprsjprs.2013.11.018.

eCognition Developer, 2015. URL: http://www.ecognition.com/suite/ecognition-developer (last accessed: July 2016).

Envisat ASAR Product Handbook, 2007. European Space Agency, Issue 2.2. available at:. https://earth.esa.int/pub/ESA_DOC/ENVISAT/ASAR/asar.ProductHandbook.2_2.pdf (last accessed: July 2016).

Fjørtoft, R., Marthon, P., Lopès, A., 1999. Multiresolution edge detection in SAR images. Presented at the Proceedings of the Norwegian Signal Processing Symposium. Tromsø, Norway.

Frost, V.S., Stiles, J.A., Shanmugan, K.S., Holtzman, J., 1982. A model for radar images and its application to adaptive digital filtering of multiplicative noise. IEEE Trans. Pattern Anal. Mach. Intell. PAMI-4:157–166. http://dx.doi.org/10.1109/TPAMI.1982.4767223.

Gholoobi, M., Tayyebi, A., Taleyi, M., Tayyebi, A.H., 2010. Comparing pixel based and object based approaches in land use classification in mountainous areas. International Archives of the Photogrammetry, Remote Sensing and Spatial Information Science, 8. Presented at the International Archives of the Photogrammetry. Remote Sensing and Spatial Information Science, Kyoto Japan, pp. 789–794.

Jacka, T.H., Giles, A.B., 2007. Antarctic iceberg distribution and dissolution from ship-based observations. J. Glaciol. 53, 341–356.

Jacobs, S.S., Jenkins, A., Giulivi, C.F., Dutrieux, P., 2011. Stronger ocean circulation and increased melting under Pine Island Glacier ice shelf. Nat. Geosci. 4:519–523. http://dx.doi.org/10.1038/ngeo1188.

Jacobs, S., Jenkins, A., Hellmer, H., Giulivi, C., Nitsche, F., Huber, B., Guerrero, R., 2012. The Amundsen Sea and the Antarctic ice sheet. Oceanography 25:154–163. http://dx.doi.org/10.5670/oceanog.2012.90.

Jacobs, S., Giulivi, C., Dutrieux, P., Rignot, E., Nitsche, F., Mouginot, J., 2013. Getz Ice Shelf melting response to changes in ocean forcing. J. Geophys. Res. Oceans 118: 4152–4168. http://dx.doi.org/10.1002/jgrc.20298.

Lancelot, C., de Montety, A., Goosse, H., Becquevort, S., Schoemann, V., Pasquer, B., Vancoppenolle, M., 2009. Spatial distribution of the iron supply to phytoplankton in the Southern Ocean: a model study. Biogeosciences 6:2861–2878. http://dx.doi.org/10.5194/bg-6-2861-2009.

Langley, K., Hamran, S.-E., Hogda, K.A., Storvold, R., Brandt, O., Hagen, J.O., Kohler, J., 2007. Use of C-band ground penetrating radar to determine backscatter sources within glaciers. IEEE Geosci. Remote Sens. Lett. 45:1236–1246 IEEE Transactions on. 10.1109/TGRS.2007.892600.

Lee, J.-S., 1981. Speckle analysis and smoothing of synthetic aperture radar images. Comput.Gr.Image Process. 17:24–32. http://dx.doi.org/10.1016/S0146-664X(81)80005-6.

Liu, Y., Moore, J.C., Cheng, X., Gladstone, R.M., Bassis, J.N., Liu, H., Wen, J., Hui, F., 2015. Ocean-driven thinning enhances iceberg calving and retreat of ice shelves. Proc. Natl. Acad. Sci. 112:3263–3268. http://dx.doi.org/10.1073/pnas.1415137112.

Mansourpour, M., Rajabi, M.A., Blais, J.A.R., 2006. Effects and performance of speckle noise reduction filters on active radar and SAR images. The International Archives of the Photogrammetry, Remote Sensing and Spatial Information Sciences, 1/W41. The International Archives of the Photogrammetry. Remote Sensing and Spatial Information Sciences, Ankara Turkey.

Mazur, A.K., Wåhlin, A.K., Krezel, A., 2016. Icebergs in the Amundsen Sea (Antarctica) determined from ENVISAT ASAR WSM data using object-based image analysis approach, link to ESRI GDB files. http://dx.doi.org/10.1594/PANGAEA.856847.

Next ESA SAR Toolbox, 2015. URL: https://earth.esa.int/web/nest/home (last accessed: July 2016).

Paolo, F.S., Fricker, H.A., Padman, L., 2015. Volume loss from Antarctic ice shelves is accelerating. Science 348:327–331. http://dx.doi.org/10.1126/science.aaa0940.

Pritchard, H.D., Ligtenberg, S.R.M., Fricker, H.A., Vaughan, D.G., van den Broeke, M.R., Padman, L., 2012. Antarctic ice-sheet loss driven by basal melting of ice shelves. Nature 484:502–505. http://dx.doi.org/10.1038/nature10968.

Raiswell, R., Benning, L., Tranter, M., Tulaczyk, S., 2008. Bioavailable iron in the Southern Ocean: the significance of the iceberg conveyor belt. Geochem. Trans. 9, 7.

Raney, R.K., 1998. Manual of remote sensing, volume 2, principles and applications of imaging radar, 3rd edition. In: Henderson, F.M., Lewis, A.J. (Eds.), Manual of Remote Sensing. Wiley Interscience, New York, NY. p. 896.

Rignot, E., Echelmeyer, K., Krabill, W., 2001. Penetration depth of interferometric synthetic-aperture radar signals in snow and ice. Geophys. Res. Lett. 28:3501–3504. http://dx.doi.org/10.1029/2000GL012484.

Rignot, E., Jacobs, S., Mouginot, J., Scheuchl, B., 2013. Ice-shelf melting around Antarctica. Science 341:266–270. http://dx.doi.org/10.1126/science.1235798.

Romanov, Y.A., Romanova, N.A., Romanov, P., 2012. Shape and size of Antarctic icebergs derived from ship observation data. Antarct. Sci. 24:77–87. http://dx.doi.org/10.1017/S0954102011000265.

Rosich, B., Meadows, P., 2004. Absolute Calibration of ASAR Level 1 Products Generated with PF-ASAR (Technical Note No. 1).

Sephton, A.J., Brown, L.M.J., Macklin, J.T., Partington, K.C., Veck, N.J., Rees, W.G., 1994. Segmentation of synthetic-aperture radar imagery of sea ice. Int. J. Remote Sens. 15: 803–825. http://dx.doi.org/10.1080/01431169408954118.

Serkan, M., Musaoglu, N., Kirkici, H., Ormeci, C., 2008. Edge and fine detail preservation in SAR images through speckle reduction with an adaptive mean filter. Int. J. Remote Sens. 29:6727–6738. http://dx.doi.org/10.1080/01431160802029644.

Silva, T.A.M., Bigg, G.R., 2005. Computer-based identification and tracking of Antarctic icebergs in SAR images. Remote Sens. Environ. 94:287–297. http://dx.doi.org/10.1016/j.rse.2004.10.002.

Smith, K.L., Robison, B.H., Helly, J.J., Kaufmann, R.S., Ruhl, H.A., Shaw, T.J., Twining, B.S., Vernat, M., 2007. Free-drifting icebergs: hot spots of chemical and biological enrichment in the Weddell Sea. Science 317, 478–483.

Stuart, K.M., Long, D.G., 2011. Tracking large tabular icebergs using the SeaWinds Ku-band microwave scatterometer. Deep-Sea Res. II 58:1285–1300. http://dx.doi.org/10.1016/j.dsr2.2010.11.004.

Tournadre, J., Whitmer, K., Ardhuin, F., 2008. Iceberg detection in open water by altimeter waveform analysis. J. Geophys. Res. 113:1–8. http://dx.doi.org/10.1029/2007JC004587.

Tournadre, J., Girard-Ardhuin, F., Legrésy, B., 2012. Antarctic icebergs distributions, 2002–2010. J. Geophys. Res. 117:2156–2202. http://dx.doi.org/10.1029/2011JC007441.

Trimble Documentation, 2014. eCognition Developer. Reference Book.

Wåhlin, A.K., Yuan, X., Björk, G., Nohr, C., 2010. Inflow of warm circumpolar deep water in the central Amundsen shelf. J. Phys. Oceanogr. 40:1427–1434. http://dx.doi.org/10.1175/2010JPO4431.1.

Wåhlin, A.K., Kalén, O., Arneborg, L., Björk, G., Carvajal, G.K., Ha, H.K., Kim, T.W., Lee, S.H., Lee, J.H., Stranne, C., 2013. Variability of warm deep water inflow in a submarine trough on the Amundsen sea shelf. J. Phys. Oceanogr. 43:2054–2070. http://dx.doi.org/10.1175/JPO-D-12-0157.1.

Wang, X., Ge, L., Li, X., 2012. Evaluation of Filters for ENVISAT ASAR speckle suppression in pasture area. ISPRS Annals of the Photogrammetry, Remote Sensing and Spatial Information Sciences. Presented at the XXII ISPRS Congress, Melbourne, Australia, pp. 341–346.

Wesche, C., Dierking, W., 2012. Iceberg signatures and detection in synthetic aperture radar (SAR) images in two test regions of the Weddell Sea, Antarctica. J. Glaciol. 58: 325–339. http://dx.doi.org/10.3189/2012JoG11J020.

Wesche, C., Dierking, W., 2015. Near-coastal circum-Antarctic iceberg size distributions determined from Synthetic Aperture Radar images. Remote Sens. Environ. 156: 561–569. http://dx.doi.org/10.1016/j.rse.2014.10.025.

Whiteside, T.G., Boggs, G.S., Maier, S.W., 2011. Comparing object-based and pixel-based classifications for mapping savannas. Int. J. Appl. Earth Obs. Geoinf. 13:884–893. http://dx.doi.org/10.1016/j.jag.2011.06.008.

Williams, R.N., Rees, W.G., Young, N.W., 1999. A technique for the identification and analysis of icebergs in synthetic aperture radar images of Antarctica. Int. J. Remote Sens. 20:3183–3199. http://dx.doi.org/10.1080/014311699211697.

Willis, C.J., Macklin, J.T., Partington, K.C., Teleki, K.A., Rees, W.G., Williams, R.G., 1996. Iceberg detection using ERS-1 Synthetic Aperture Radar. Int. J. Remote Sens. 17: 1777–1795. http://dx.doi.org/10.1080/01431169608948739.

Young, N.W., Turner, D., Hyland, G., Williams, R.N., 1998. Near-coastal iceberg distribution in East Antartica, 50-145° E. Ann. Glaciol. 27, 69–74.